# Flexible Solar-Energy Harvesting System on Plastic with Thin-film LC Oscillators Operating Above $f_t$ for Inductively-coupled Power Delivery

Yingzhe Hu, Warren Rieutort-Louis, Liechao Huang, Josue Sanz-Robinson
Sigurd Wagner, James C. Sturm, Naveen Verma
*Princeton University, Princeton (NJ), USA*

*Abstract*- **This paper presents an energy-harvesting system consisting of amorphous-silicon (a-Si) solar cells and thin-film-transistor (TFT) power circuits on plastic. Along with patterned planar inductors, the TFTs realize an LC-oscillator that provides power inversion of the DC solar-module output, enabling a low-cost sheet for inductively-coupled wireless charging of devices. Despite the low performance of the TFTs ($f_t$=1.3MHz at a voltage of 15V), the oscillator can operate above 2MHz by incorporating the device parasitics into the resonant tank. This enables increased quality factor for the planar inductors, improving the power-transfer efficiency and the power delivered. With 3cm-radius single- and double-layer inductors, the system achieves 22.6% and 31% power-transfer efficiency (approaching the analytically-predicted bound), while the power delivered is 20mW and 22mW.**

## I. INTRODUCTION

Thin-film electronics can be processed at low temperatures enabling the integration of diverse transducers with functional circuits on large, flexible sheets. This can lead to transformational systems for high-resolution sensing [1] and energy harvesting [2]. A critical limitation, however, is the low performance of thin-film transistors (TFTs), which typically have $f_t$ around 1MHz. LC oscillators are a key building block in circuits for communication, control, and power conversion. An important characteristic is that they can operate above $f_t$ and could thus play a key role in overcoming the limitations of thin-film systems.

In this work, we present a thin-film energy-harvesting system based on amorphous-silicon (a-Si) solar modules and TFTs. In contrast to previous work [2], we demonstrate energy-harvesting devices and power circuits in the same technology, thus enabling a path to low-cost, fully-integrated sheets for ubiquitous power conversion and delivery. Such sheets could be applied onto existing surfaces to convert them into charging stations for wireless powering of mobile devices. Compared to other designs [3], the proposed approach uses inductors rather than capacitors for coupling power to load devices. This enables greater power transfer for a given size (i.e., by a factor of 200 compared to [3]) as well as superior robustness to variations in proximity [4]. The key challenge with inductors, however, is reduced quality factor at low frequencies. We thus employ a thin-film LC oscillator as a power inverter to convert the DC solar-module outputs into AC waveforms, enabling inductive coupling at higher frequencies than that limited by $f_t$. The resulting topology also avoids the need for explicit switching control circuits, thus overcoming limitations to both performance and efficiency imposed by the TFTs. In the following sections, we analyze circuit tradeoffs, taking into account inherent component-level parasitics, which lead to a design-optimization methodology.

## II. SYSTEM OVERVIEW

Fig. 1 shows a block diagram of the energy-harvesting system. The solar module consists of solar cells in series operating at an output voltage $V_{op}$ of 10-25V. Although LC oscillators offer the benefits mentioned, in order to function, they must have sufficient gain to meet the positive-feedback condition. This depends partially on device characteristics related to $f_t$ (i.e., transconductance and capacitances), which are not favorable for TFTs; however, it also depends on the inductance-to-resistance ratio achievable with patterned planar inductors. We thus exploit the ability to create physically-large inductors on plastic, which can lead to large values of this ratio, enabling oscillations despite poor TFT characteristics.
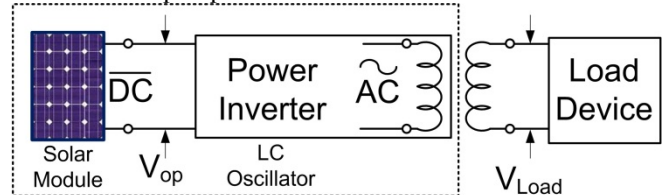


**Fig. 1: Block diagram of thin-film energy-harvesting system.**

Fig. 2 (left) shows the LC-oscillator including the circuit parasitics of importance. In addition to the TFT capacitances, the TFT gate resistances ($R_{gate}$) and inductor resistances ($R_{ind}$) are included. The gate resistances and capacitances are modeled as lumped elements since the frequencies of interest are much lower than that due to the associated time constant (which is several giga-Hertz). Nonetheless, $R_{gate}$ is significant for the analysis due to the use of a bottom-gate TFT structure (as described in Sec. IV), which requires thin gate metallization in order to ensure reliable gate dielectric formation. At resonance, the parasitics can be represented as shown in Fig. 2 (right), where $R_{Par}$ can be estimated by

$$R_{Par} \approx Q^2(R_{ind} + R_{gate}) = \frac{\omega^2 L^2}{R_{ind}+R_{gate}} = \frac{L}{C_{Par}(R_{ind}+R_{gate})}, \quad (1)$$

and $C_{Par}$ can be estimated by taking into account Miller multiplication effects:

$$C_{Par} = 2 \times (C_{gd1} + C_{gd2}) + C_{gs1,2} + C_{ox} \approx 5 \times C_{ov} + C_{ox}. \quad (2)$$
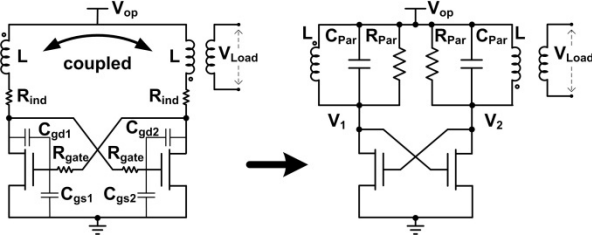
**Fig. 2: LC oscillator with parasitics and equivalent circuit for analysis.**

With TFT output resistances being much larger than typical values for $R_{Par}$, the positive-feedback condition requires that $g_m \times R_{Par} > 1$, leading to the following requirement:

$$\frac{g_m}{C_{Par}} \times \frac{L}{(R_{ind} + R_{gate})} > 1. \tag{3}$$

While the first term on the left represents a dependence related to device $f_t$, the second term suggests that this can be overcome by a suitable inductor. Fig. 3 plots $L/(R_{ind} + R_{gate})$ values, both from measurement (using prototyped inductors) and from simulated prediction (using [5]). Fabricated TFTs achieve a measured $f_t$ of 1.3MHz (i.e., $g_m/C_{par} = 4.2 \times 10^6$ rad/s ) at 15V, thus suggesting that the oscillation condition of Eq. 3 can be met with sufficient margin.
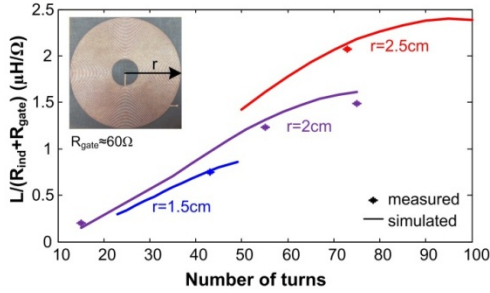


**Fig. 3: $L/(R_{ind}+R_{gate})$ ratios for prototyped planar inductors.**

III. POWER INVERTER ANALYSIS AND OPTIMIZATION

Given the viability of thin-film LC oscillators, this section analyzes their efficiency and power-transfer capabilities when used as power inverters with an inductively-coupled load. As shown in Fig. 2, power is delivered to a single load by coupling the inductors in the two LC tank branches. The load causes an associated resistance to be reflected to the oscillator outputs. For analysis, as in Fig. 4, we use an equivalent topology, with equal-valued inductors for each oscillator branch, independently coupled to load inductors with nearly-perfect coupling efficiency (i.e., $k \approx 1$, which is reasonable for proximity power transfer). A reflected load ($R_{Load}$) hence appears in each branch. This has two effects: (1) $R_{Load}$ impacts the positive-feedback condition, effectively altering the oscillation amplitude; and (2) $R_{Load}$ splits the power extracted from the LC tank with $R_{Par}$ in order to achieve the desired power delivery. These effects result in a design optimization methodology for maximum output power and efficiency. To analyze this, we define an oscillator strength parameter $S$; $S$ is derived from the oscillation condition, and, as described in the following subsections, it suggests how the designer-selectable parameters, $R_{Load}$ and $g_m$, should be set to maximize output power and efficiency:

$$S = g_m \times (R_{Load} \parallel R_{Par}). \tag{4}$$

An additional parameter of importance is the operating-point voltage of the solar-module ($V_{op}$), which affects both the absolute output power and efficiency that can be achieved.
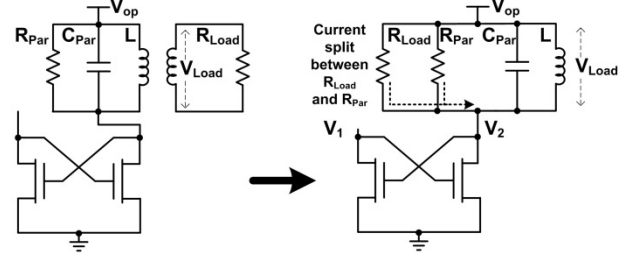


W/L=3600µm/6µm, R_{gate}≈60Ω, C_{gd}/C_{gs}=5pF, C_{ox}=5pF, L_{ind}=200µH, R_{ind}=35Ω

**Fig. 4: Oscillator circuit with reflected load resistance; parameter values from a fabricated sample are shown for illustration.**

*A. Power-transfer Optimization*

This section describes how the designer-selectable parameters should be set to optimally achieve a desired output power. For each oscillator branch, the power delivered to the load is:

$$P_{out} = \frac{V_{Load}^2}{2 \times R_{Load}}, \tag{5}$$

where $V_{Load}$ is the amplitude of the AC oscillations. Eq. 5 suggests that $R_{Load}$ should be minimized for maximum power transfer; however, due to its impact on $S$, $R_{Load}$ affects $V_{Load}$. In order to sustain oscillations, reducing $R_{Load}$ thus requires $g_m$ to be increased. This can be achieved in two ways: (1) by increasing $V_{op}$, which raises the gate-overdrive of the TFTs; or (2) by increasing the W/L of the TFTs. Fig. 5(a) shows the effect of increasing $V_{op}$ (based on transistor-level simulations using extracted SPICE Level 61 models for the TFTs; measurement results are also shown for $V_{op} = 20V$ to illustrate validity of the models). Due to the increased $g_m$, nearly full-swing oscillations can be achieved at reduced values of $R_{Load}$ (as determined by $S$). Although increasing $R_{Load}$ increases $V_{Load}$ further, the effect saturates once sufficient $S$ is achieved. Combined with the inverse dependence in Eq. 5, Fig. 5(b) shows that an optimal point thus occurs by balancing $R_{Load}$. The resulting optimal $R_{Load}$ shown corresponds to a value of $S \approx 3.5$; however, as discussed in Sec. III-B, efficiency optimization requires a higher value ($S \approx 5$) for $V_{Load}$ saturation. Nonetheless, with regards to $P_{Load}$, increasing $V_{op}$ also increases the achievable $V_{Load}$, causing the effect in Fig. 6(a), where $P_{Load}$ scales roughly cubically (as predicted by Eq. 5).
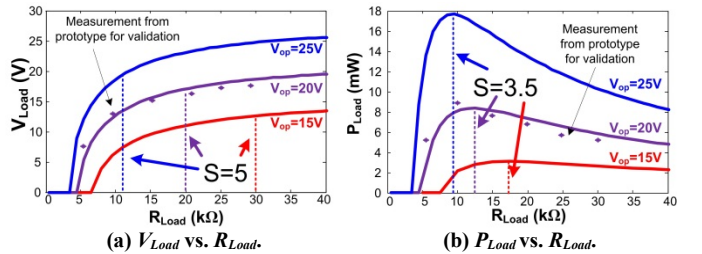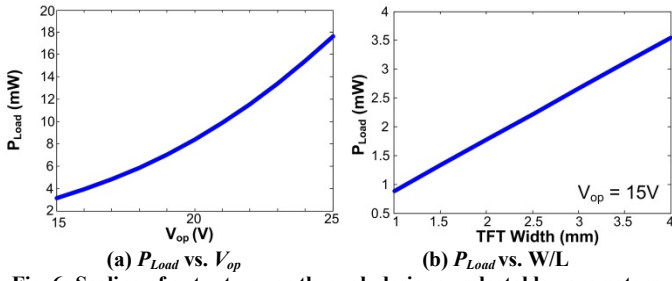


**(a) $V_{Load}$ vs. $R_{Load}$.**    **(b) $P_{Load}$ vs. $R_{Load}$.**
**Fig. 5: Effect of $R_{Load}$ scaling on oscillation amplitude and output power.**

Similarly, increasing W/L increases $g_m$, enabling oscillations to be sustained at a lower $R_{Load}$. However, raising W/L also increases $C_{Par}$, thereby reducing $R_{Par}$ in proportion.

**(a) $P_{Load}$ vs. $V_{op}$**   **(b) $P_{Load}$ vs. W/L**

**Fig. 6: Scaling of output power through designer-selectable parameters.**

As a result, $S$ remains unchanged, causing $V_{Load}$ to also remain unchanged. As shown in Fig. 6(b), $P_{Load}$ thus scales linearly (due to $R_{Load}$).

*B. Efficiency Optimization*

This section first examines the power consumed by the LC oscillator, and then uses this with the output power to analyze the power-transfer efficiency. Although the solar module's output voltage ($V_{op}$) and current are coupled, the circuit operates in a region close to the open-circuit module voltage, hence we approximate the average power consumed as

$$P_{avg} = V_{op} \times I_{TFT,avg}, \qquad (6)$$

where $I_{TFT,avg}$ is the average current drawn by each TFT. During each cycle, the $V_{gs}$ and $V_{ds}$ of the TFTs oscillate in counter phase. For large oscillations of $V_{Load}$, the instantaneous TFT current ($I_{TFT}$) is thus near zero both when $V_{gs}$ is maximum (due to low $V_{ds}$) and when $V_{ds}$ is maximum (due to low $V_{gs}$). As shown in the simulation of Fig. 7(a), $I_{TFT}$ is maximized when $V_{gs}=V_{ds}=V_{op}$, and the average current is thus roughly half this. As a result, the $g_m$ in Eq. 4 is related to $I_{TFT,avg}$ as follows:

$$I_{TFT,avg} = \tfrac{1}{4} g_m (V_{op} - V_t). \qquad (7)$$

Fig. 7(b) shows $I_{TFT,avg}$ with respect to $R_{Load}$ (plotted for the circuit parameters in Fig. 4). $I_{TFT,avg}$ begins to saturate as $R_{Load}$ is increased. This occurs due to increasing $V_{Load}$, which causes the current waveform ($I_{TFT}$) to reach the extreme values described above. This corresponds to $S\approx5$.



**(a) $V_{Load}$ and $I_{TFT}$ waveforms.**   **(b) $I_{TFT,avg}$ vs. $R_{Load}$.**
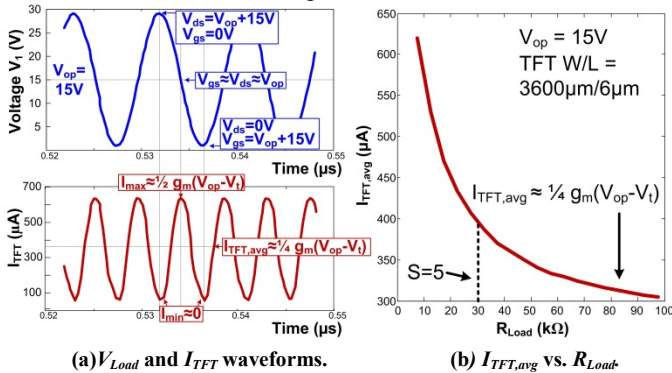
**Fig. 7: Transistor-level simulation of the effect of $R_{Load}$ on TFT current.**

Now, the oscillator efficiency can be expressed as follows

$$\eta = \frac{\frac{V_{Load}^2}{2 \times R_{Load}}}{V_{op}I_{TFT,avg}} = \frac{\left(\frac{V_{Load}^2}{2 \times (R_{Load}\|R_{par})}\right)}{V_{op}I_{TFT,avg}} \times \frac{R_{Par}}{R_{Par}+R_{Load}} = \eta_{osc} \times \eta_{tank}, \quad (8)$$

where two effective efficiencies are explicitly defined: $\eta_{osc}$ corresponds to the efficiency of maintaining oscillations in the

presence of $R_{Par}$ and $R_{Load}$ (i.e., ensuring sufficient $S$); and $\eta_{tank}$ corresponds to the efficiency with which current is delivered to $R_{Load}$ versus $R_{Par}$.

From Eq. 8, the impact on $\eta$ due to $R_{Load}$ and $g_m$ can be understood. In addition to its explicit impact, $R_{Load}$ has an implicit effect through $V_{Load}$ and thus $I_{TFT,avg}$; the profile in Fig. 5(a) shows the saturating effect of $R_{Load}$ on $V_{Load}$. Thus, combined with the effect on $I_{TFT,avg}$ and the inverse impact of $R_{Load}$ on $\eta$, the efficiency exhibits the optimal values shown in Fig. 8(a) at $S\approx5$.

On the other hand, increasing $g_m$ through W/L sizing causes a linear increase in $P_{Load}$ (Fig. 6(b)), but also a linear increase in $I_{TFT,avg}$, due to TFT width scaling. As a result, $\eta$ exhibits no net change with W/L. To understand the effect of increasing $V_{op}$, it is helpful to look at $\eta_{osc}$ and $\eta_{tank}$ separately. For $\eta_{osc}$, the achievable $V_{Load}$ is increased linearly, $I_{TFT,avg}$ is increased quadratically (assuming square-law TFT behavior), and $R_{Load}\|R_{Par}$ can be decreased linearly for a required value of $S$ (thanks to increased $g_m$); as a result, $\eta_{osc}$ remains unchanged. However, the reduction allowed to $R_{Load}$, improves $\eta_{tank}$. As a result, the overall $\eta$ initially improves, as shown in Fig. 7(b); however, this improvement eventually saturates according to the expression for $\eta_{tank}$.



**(a) $\eta$ vs. $R_{Load}$.**   **(b) $\eta$ vs. $V_{op}$.**
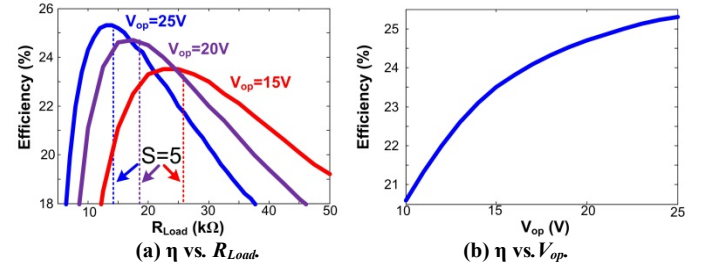
**Fig. 8: Simulations of harvester efficiency with respect to $R_{Load}$ and $V_{op}$.**

Given these effects, we can estimate a bound for the maximum overall efficiency achievable by the topology. Using Eqs. 4, 7, and 8, and assuming, $V_{op}\gg V_t$ and $V_{Load}\approx V_{op}$

$$\eta_{max} \approx \frac{V_{op}^2 \times \frac{g_m}{S}}{2V_{op} \times \frac{1}{4}g_m V_{op}} = \frac{2}{S} \approx 40\%, \qquad (9)$$

where $S\approx5$ has been used based on discussed optimizations.

## IV. EXPERIMENTAL RESULTS

The energy-harvesting system is fabricated on 50μm-thick flexible polyimide foil using patterned inductors of several sizes (i.e., radii of 2, 2.5, and 3 cm). A photograph of a sample is shown in Fig. 9. TFTs with W/L of 3600μm/6μm are used, and the layout is optimized for minimum gate-source/drain capacitance, since maximizing $g_m/C$ ratio is critical for the positive-feedback condition of Eq. 3. For TFTs with 5μm gate-source/drain overlap, an $f_t$ of 1.3MHz (at 15V) is measured. Further reduction in overlap is unreliable for lithographic alignment on plastic.
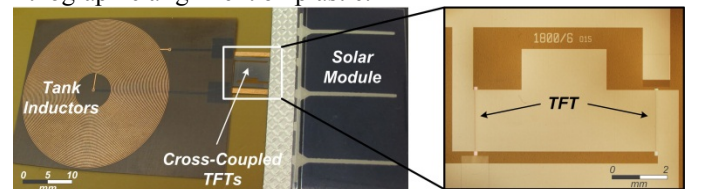


**Fig 9: Micrograph of energy-harvesting system on flexible foil.**

Typical oscillator waveforms from measurement are in Fig. 10; while nearly full swing oscillations are achieved at 2MHz, oscillations with reduced amplitude are also observed at 3.64MHz. A performance summary is shown in Table I.
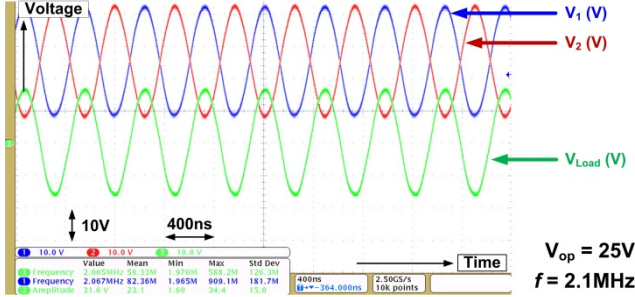


**Fig. 10: Measured waveforms from system captured via oscilloscope.**

**Table I: Prototype system performance (shown for $V_{op}$ =15V, 25V).**

| Inductor size | radius= 2, 2.5, 3cm | | |
|---|---|---|---|
| TFT W/L | 3600μm / 6μm | | |
| $f_t$ | 1.3MHz ($V_{op}$=15V) | | |
| Max. Freq. | 2.1MHz ($V_{Load}$=16V), 3.64MHz ($V_{Load}$=5V) | | |
| $V_{op}$ | 15 | 25 | 25 (2-layer inductor) |
| Solar Modules | 180cm² | 300cm² | 300cm² |
| Optimal $R_{Load}$ | 20kΩ | 8kΩ | 2kΩ |
| Max. $P_{LOAD}$ | 2.6mW | 20.3mW | 22.1mW |
| Max. η | 15.4% | 22.6% | 31% |

Fig. 11 shows the structure of a-Si NMOS TFTs as well as a measured typical I-V characteristic. Fabrication is achieved by PECVD deposition at low temperature (180°C), enabling the use of a polyimide foil substrate. For robustness under flexing, metal layers use chrome-aluminum-chrome stacks.
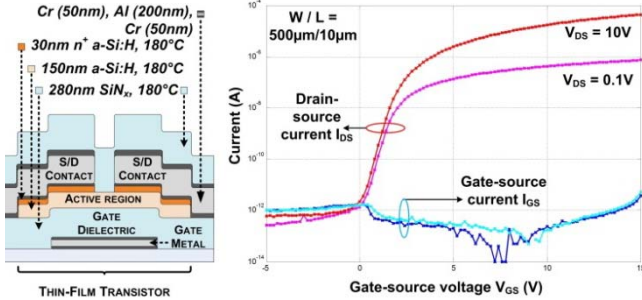


**Fig. 11: Low-temperature processing of a-Si NMOS TFTs.**

*A. Power and Overall Efficiency versus $R_{Load}$*

The measured output power delivered to a load ($P_{Load}$) and the overall efficiency (η) are shown in Fig. 12. Optimal values exist, as described in Sec. III-A & III-B. Additionally, physically-larger inductors lead to larger $R_{Par}$, improving $η_{tank}$, and thereby increasing the overall efficiency.



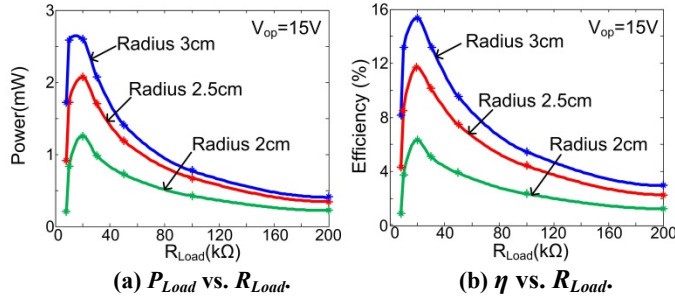**(a) $P_{Load}$ vs. $R_{Load}$.**  **(b) η vs. $R_{Load}$.**

**Fig. 12: Output power and efficiency measurements with $R_{Load}$.**

*B. Power and Overall Efficiency versus $V_{op}$*

Fig. 13(a) shows $P_{Load}$ with respect to $V_{op}$ (for an optimal $R_{Load}$), Fig. 13(b) shows η with respect to $V_{op}$ and $R_{Load}$, and Fig. 13(c) shows the optimal η with respect to $V_{op}$ (for an inductor radius of 3cm). As described in Sec. III-A, Fig. 13(a) shows that $P_{Load}$ increases approximately cubically with $V_{op}$. Larger inductors result in improved $P_{Load}$ for the same reason as in Section IV-A. Further, as mentioned in Sec. III-B, η initially increases with $V_{op}$ due to resulting improvement in $η_{tank}$ through reduced $R_{Load}$. Since Fig. 13(c) approaches the voltage limit of the TFTs, to further explore this effect, we increase $η_{tank}$ by explicitly increasing $R_{Par}$. $R_{Par}$ can be increased by further increasing the inductor size or by stacking inductors in multiple layers; this causes the number of turns to effectively double, increasing L by a factor of four, while causing $R_{ind}$ to increase by only a factor of two. The third column of Table I shows the measured results, demonstrating power-transfer efficiency approaching the bound of Eq. 9.
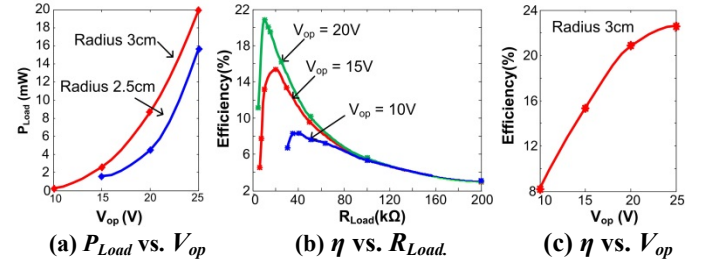


**(a) $P_{Load}$ vs. $V_{op}$**  **(b) η vs. $R_{Load}$.**  **(c) η vs. $V_{op}$**

**Fig. 13: Efficiency measurements with respect to $V_{op}$.**

V. CONCLUSIONS

Thin-film systems face performance limitations due to the $f_t$ limit of the TFTs. LC oscillators can resonate device capacitances with the tank inductors, enabling operation beyond the $f_t$. This, however, requires inductors with sufficiently small resistances. Thin-film systems fabricated on plastic substrates can achieve this through physically-large planar inductors that can be patterned on large substrates. We thus demonstrate operation of a thin-film LC oscillator above device $f_t$. We exploit this to then create an energy-harvesting system that uses an LC-oscillator-based power inverter to convert a DC solar-module output into an AC waveform for inductively-coupled wireless power delivery to load devices. The oscillator operates at a maximum frequency of 2.1MHz, and the system achieves an output power of up to 22mW, with a maximum power-transfer efficiency of 31%, which approaches the predicted maximum value for the topology.

REFERENCES

[1] T. Someya, et al., "Organic Semiconductor Devices with Enhanced Field and Environmental Responses for Novel Applications," *MRS Bulletin*, 2008
[2] K. Ishida, et al., "Insole Pedometer with Piezoelectric Energy Harvester and 2V Organic Digital and Analog Circuits," *ISSCC*, Feb. 2012.
[3] L. Huang, et al., "Integrated All-silicon Thin-film Power Electronics on Flexible Sheets For Ubiquitous Wireless Charging Stations based on Solar-energy Harvesting", *VLSI Symp. Circuits*, June 2012 (in press).
[4] N. Miura, et al., "Analysis and design of inductive coupling and transceiver circuit for inductive inter-chip wireless superconnect" *Journal of Solid-State Circuits*, April 2005
[5] P. Nicholson, "ACMI Air Core Mutual Inductance Calculator" http://abelian.org/acmi/